

DISCOVERY OF A TIME LAG BETWEEN THE SOFT X-RAY AND RADIO EMISSION OF THE TIDAL
DISRUPTION FLARE ASASSN-14LI: EVIDENCE FOR LINEAR DISK–JET COUPLINGDHEERAJ R. PASHAM¹

Massachusetts Institute of Technology, Cambridge, MA, 02139

AND

SJOERT VAN VELZEN²Department of Physics & Astronomy, Johns Hopkins University, Baltimore, MD 21218 and
Center of Cosmology and Particle Physics, New York University, New York, NY 10003*Draft version August 28, 2018*

ABSTRACT

The tidal disruption of a star by a supermassive black hole can result in transient radio emission. The electrons producing these synchrotron radio flares could either be accelerated inside a relativistic jet or externally by shocks resulting from an outflow interacting with the circumnuclear medium. Until now, evidence for the internal emission mechanism has been lacking; nearly all tidal disruption flare studies have adopted the external shock model to explain the observed properties of radio flares. Here we report a result that presents a challenge to external emission models: we discovered a cross-correlation between the soft X-ray (0.3–1 keV) and 16 GHz radio flux of the tidal disruption flare ASASSN-14li. Variability features in the X-ray light curve appear again in the radio light curve, but after a time lag of 12^{+6}_{-5} days. This demonstrates that soft X-ray emitting accretion disk regulates the radio emission. This coupling appears to be inconsistent with all previous external emission models for this source but is naturally explained if the radio emission originates from a freely expanding jet. We show that emission internal to an adiabatically expanding jet can also reproduce the observed evolution of the radio spectral energy distribution. Furthermore, both the correlation between X-ray and radio luminosity as well as our radio spectral modeling imply an approximately linear coupling between the accretion rate and jet power.

1. INTRODUCTION

The tidal disruption of a star by a massive black hole ($\gtrsim 10^4 M_\odot$) can lead to a spectacular flare that is observable across the entire electromagnetic spectrum. Thermal, i.e., blackbody emission, is detected at optical/UV (Gezari et al. 2009; van Velzen et al. 2011; Arcavi et al. 2014) and soft X-ray (Bade et al. 1996; Esquej et al. 2008) frequencies and is thought to originate from the tidal debris of the star (e.g., Pasham et al. 2017, ; P+17 hereafter). Dust reprocessing of this thermal flare can yield a transient signal at mid-infrared wavelengths (e.g., van Velzen et al. 2016a).

A handful of candidate stellar tidal disruption flares (TDFs; Bloom et al. (2011)) that have been discovered by their thermal emission are also detected at radio frequencies: ASASSN-14li (van Velzen et al. 2016b; Alexander et al. 2016), XMMSL1 J074085 (Saxton et al. 2017; Alexander et al. 2017), and IGR J12580+0134 (Irwin et al. 2015; Perlman et al. 2017)—although the last is perhaps more likely explained by the activity of a pre-existing active galactic nucleus (see Auchettl et al. 2017 for further discussion). The radio luminosities of these sources are $\sim 10^{38} \text{ erg s}^{-1}$ and fade with a characteristic time scale of a few months. The equipartition energy of the observed radio emission from ASASSN-14li is $\sim 10^{48} \text{ erg}$ (Alexander et al. 2016). This rather low energy and short lifetime leaves open the possibility that such low-luminosity radio flares are common for thermal

TDFs. Most radio follow-up observations (e.g., Bower et al. 2013; van Velzen et al. 2013) were simply not sensitive enough to detect such events; however see Blagorodnova et al. (2017) for a recent counterexample.

The radio luminosity of the thermal TDFs is over three orders of magnitude lower than the radio luminosity of the TDFs that have been discovered by their non-thermal γ -ray emission (Bloom et al. 2011; Zauderer et al. 2011; Levan et al. 2011; Zauderer et al. 2011; Burrows et al. 2011; Cenko et al. 2012; Brown et al. 2015; Pasham et al. 2015). The non-thermal X-ray emission of these TDFs is best explained by Doppler-boosted emission caused by a relativistic jet observed at a small inclination. Synchrotron emission due to electrons accelerated in the forward shock of this jet can explain the observed radio light curves (Giannios & Metzger 2011; Metzger et al. 2012; Berger et al. 2012; Mimica et al. 2015; Generozov et al. 2017). This external emission mechanism is akin to models for radio afterglows of γ -ray bursts (e.g., Piran 2004; Nakar & Piran 2011) or supernovae (Chevalier 1998). The isotropic energy of the jet that powers the non-thermal TDFs is $\sim 10^{53} \text{ erg}$ (e.g., Mimica et al. 2015).

An external emission model could also explain the observed radio light curves of thermal TDFs. If the accretion onto the black hole exceeds its Eddington limit, we might anticipate the launch of a photon-driven wind (e.g., Sądowski & Narayan 2016). When this wind interacts with the circumnuclear medium, shocks can accelerate electrons to yield synchrotron emission (Alexander et al. 2016, 2017). An alternative scenario has been pro-

¹ NASA Einstein Fellow; dheeraj@space.mit.edu² NASA Hubble Fellow; sjoert@nyu.edu

posed by Krolik et al. (2016), who suggests that shocks driven by the unbound stellar debris streams are responsible for producing the synchrotron-emitting electrons. Finally, a third possibility is that the radio emission originates from a forward shock of a relativistic jet that is being decelerated by the circumnuclear medium (van Velzen et al. 2016b).

We are thus presented with a dichotomy of radio power from TDFs (Generozov et al. 2017): low-power thermal TDFs and high-power non-thermal TDFs. However, since the nature of radio emission of the radio-weak TDFs is still under debate, interpreting this dichotomy is difficult. If the radio-weak TDFs are also due to a jet, a unified picture emerges in which all tidal disruptions lead to jet launching (van Velzen et al. 2011), and the observed radio power dichotomy translates into a jet power dichotomy. On the other hand, if radio-weak TDFs are explained by a disk-wind or unbound debris, the observed radio power dichotomy could be explained by the initial conditions that are required for the launch of a relativistic jet (e.g., Tchekhovskoy et al. 2014).

The goal of this work is to carry out a cross-correlation analysis between the X-ray and the radio light curves of ASASSN-14li to understand the nature of the radio emission of this thermal TDF. Below we first briefly introduce this “Rosetta stone” TDF. We then present the details of its radio and X-ray observations in Sec. 2, followed by the cross-correlation analysis in Sec. 3. We then discuss our new jet model for the synchrotron emission of this source in Sec. 4 and close with a discussion in Sec. 5.

1.1. ASASSN-14li

The optical transient ASASSN-14li was discovered by the All-Sky Automated Survey for SuperNovae (ASASSN; Shappee et al. 2014) on 22 November 2014 or MJD 56983.6 (?). Within a few weeks it became clear that this source displayed nearly all the known properties of previous optical TDFs: an origin consistent with the nucleus of the host galaxy, an optical spectrum with broad hydrogen and helium emission lines, and a constant blue optical/UV color, corresponding to a temperature of roughly 3×10^4 K (Holoien et al. 2016).

Two properties are unique to ASASSN-14li: the detection of a luminous, thermal X-ray flare (Miller et al. 2015) and the detection of a low-luminosity ($\approx 10^{38}$ erg s $^{-1}$ at 16 GHz) radio flare (van Velzen et al. 2016b; Alexander et al. 2016). The size of the X-ray emitting region as inferred from energy spectral modeling and fast time variability is only a few gravitational radii (Miller et al. 2015). This small radius, combined with the fact that the X-ray spectrum is thermal, suggests that the X-rays originate from the innermost regions of the accretion flow (Krolik et al. 2016). Because relativistic ejections—which can produce synchrotron radio emission—are also launched from close to the black hole, ASASSN-14li provides a unique laboratory to understand the connection, if any, between the accretion and the ejection of matter near a black hole.

Thanks to its very low redshift, observations with European VLBI Network (EVN) could spatially resolve the radio emission from ASASSN-14li (Romero-Cañizales et al. 2016). The 5 GHz EVN observations, taken about 200 d after its discovery, revealed a stationary feature

TABLE 1
SUMMARY OF X-RAY SPECTRAL MODELING.

MJD Range	N_{H} (10^{22} cm $^{-2}$)	T (keV)	χ^2/dof
56991-57014	$0.106^{+0.034}_{-0.033}$	$0.053^{+0.004}_{-0.004}$	1.843/32
57016-57037	$0.082^{+0.032}_{-0.028}$	$0.057^{+0.004}_{-0.004}$	1.224/31
57039-57072	$0.109^{+0.034}_{-0.031}$	$0.054^{+0.004}_{-0.004}$	1.371/32
57075-57137	$0.094^{+0.040}_{-0.053}$	$0.048^{+0.007}_{-0.006}$	0.717/28
57139-57192	$0.015^{+0.028}_{-0.015}$	$0.055^{+0.004}_{-0.005}$	1.416/28
57195-57367	$0.069^{+0.049}_{-0.037}$	$0.044^{+0.005}_{-0.005}$	1.319/24
57370-57834	$0.176^{+0.218}_{-0.109}$	$0.026^{+0.008}_{-0.008}$	1.722/17

NOTE. — N_{H} , and T are the best-fit hydrogen column and the blackbody temperature, respectively, of ASASSN-14li’s 0.3–1.0 keV average X-ray spectra. The reduced χ^2 along with the degrees of freedom (dof) for the X-ray spectral fit are shown in the last column.

with a size of a few milliarcseconds (mas) and a second component ≈ 2 parsecs away with a factor of 6 lower in flux.

The host galaxy of ASASSN-14li (redshift = 0.0206 or 90 Mpc) is a post-starburst galaxy; TDFs happen preferentially in these rare types of galaxies (Arcavi et al. 2014; French et al. 2016). Integral field spectroscopic observations of the host revealed ionized filaments, similar to ionization nebulae around fading AGNs (Prieto et al. 2016). Indeed the detection of low-luminosity radio emission prior to the tidal disruption is best explained by a low-luminosity AGN (Holoien et al. 2016; van Velzen et al. 2016b; Alexander et al. 2016).

2. RADIO AND X-RAY OBSERVATIONS

2.1. Radio Data

The radio data used in this work were acquired by three different telescopes. The Arcminute Microkelvin Imager (AMI) and the Westerbork Synthesis Radio Telescope (WSRT) provided 15.7 GHz and 1.4 GHz radio data, respectively (van Velzen et al. 2016b). Further multi-epoch radio spectral energy distribution (SED) data were acquired by the very large array (VLA) (Alexander et al. 2016). AMI started monitoring ASASSN-14li at 15.7 GHz 31 d after its discovery (van Velzen et al. 2016b). The radio campaign lasted about 140 d with an observing cadence of about one visit every four days. All the radio data used here are as published by van Velzen et al. (2016) and Alexander et al. (2016).

The pre-flare radio flux of ASASSN-14li, based on archival data, is orders of magnitude higher than what is expected from star formation alone. This indicates that a weak AGN was present prior to the flare (Holoien et al. 2016; van Velzen et al. 2016b; Alexander et al. 2016). From the plateau in the late-time AMI light curve we infer that the baseline (i.e., non-transient) flux at 15.5 GHz is 0.24 mJy (Bright et al. 2018). To model the observed non-transient flux ($S_{\nu, \text{baseline}}$) at other frequencies (ν), one has to account for the source spectrum as well as the difference in angular resolution (or beam) between telescopes and observed frequencies. Here we adopt a simple power-law model with a typical spectral index of

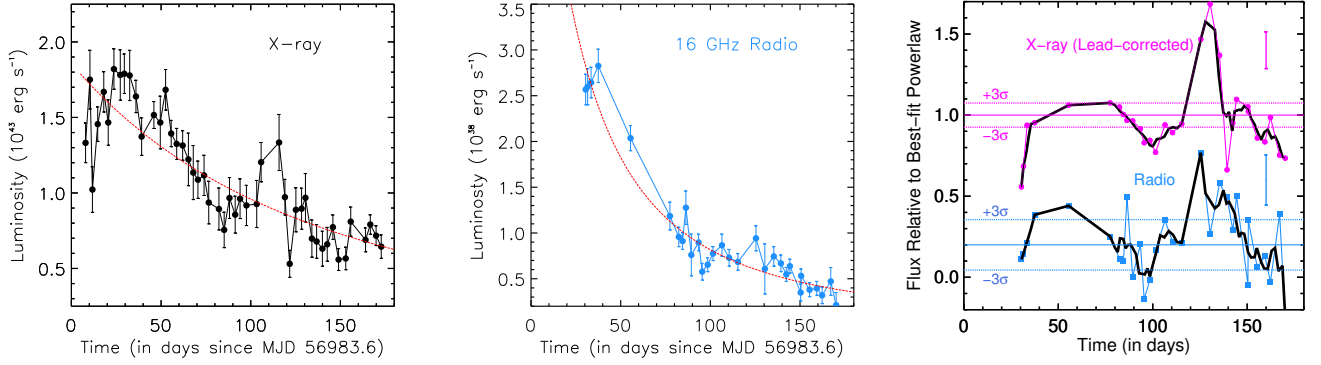


FIG. 1.— De-trending the light curves. *Left:* ASASSN-14li’s X-ray (0.3–1.0 keV) light curve (magenta data points) along with the best-fit power-law decay model (dashed black curve). *Center:* The 15.7 GHz transient radio light curve (blue data points) and its best-fit power-law decay model (dashed red curve). The error bars represent the 1σ confidence interval (including the systematic uncertainty of converting from count rate to luminosity). A constant value of 0.24 mJy was subtracted from the observed 15.7 GHz light curve to exclude the non-transient component (see Sec. 2.1). *Right:* The relative X-ray (magenta) and radio (blue) light curves obtained by dividing their corresponding best-fit power-law model. X-ray and the radio fractional variability amplitudes on top of the power-law decay are $10\pm 1\%$ and $16\pm 1\%$, respectively. The mean flux levels are shown by the solid horizontal lines. The radio data has been vertically offset by -0.8 . The solid black curves are running averages over a 10 d window (except when the gap between observations is longer than 10 d). Typical 1σ uncertainties derived from the left and middle panels are shown as vertical bars. The dashed horizontal lines are the $\pm 3\sigma$ variability contours derived using the methodology described in Romero-Cañizales et al. (2011). The X-ray data points shown here have been interpolated to match with the radio epochs (see Sec. 3.1). Uncertainty on the time lag after fully accounting for these error bars can be found in the middle and right the panels of Fig. 2.

-0.8 (e.g., Ker et al. 2012):

$$S_{\nu, \text{baseline}} = 0.24 \left(\frac{\nu}{15.7 \text{ GHz}} \right)^{-0.8} \text{ mJy} \quad (1)$$

This spectrum is expected if the non-transient radio flux is due to a lobe that was created by the jet that was active prior to the disruption. Our model for the baseline flux (Eq. 1) is consistent with the 5 GHz VLA flux that is resolved-out in the EVN observations (Romero-Cañizales et al. 2016), suggesting that the region that contains the majority of the baseline emission is smaller than the resolution of the VLA observations at this frequency ($\approx 1''$). Hence the beam difference between AMI and the VLA is expected to have only a modest influence on the observed baseline flux.

2.2. X-ray Data Reduction

Roughly a week after its discovery, *Swift* started monitoring ASASSN-14li with a mean observing cadence of one visit (1–3 ks) every three days. This cadence was maintained for about 270 days but the monitoring campaign suffered from longer data gaps thereafter because of sun angle constraints. To ensure that the cross-correlation function (CCF) is not heavily biased by the X-ray data points, we only used the first 180 days of X-ray data (similar in temporal baseline as AMI data) for evaluating the CCF between the X-ray and the 15.7 GHz AMI data. X-ray data were first analyzed by Holoien et al. (2016) and Miller et al. (2015). However, to properly account for pile-up and estimate the flux we re-analyzed the entire *Swift* data, as discussed in detail below.

We reduced the XRT data and extracted pile-up corrected X-ray spectra from each XRT observations following the analysis procedure outlined in P+17. The unner exclusion radius to mitigate pileup was estimated separately from each XRT exposure by modeling the point spread function (PSF) using the method outlined in the

Swift/XRT user guide³. The inner exclusion radii estimated in this manner are given in the last but one column of Table A1.

The X-ray spectrum of ASASSN-14li is very soft with almost all counts between 0.3 and 1.0 keV, and is well-fit with a blackbody model (Miller et al. 2015). Therefore, we modeled its X-ray spectra with a blackbody function. The individual *Swift*/XRT monitoring observations lack the necessary signal-to-noise to constrain the blackbody temperature and radius. To be able to constrain the model parameters in each XRT observation, we carried out an analysis similar to the approach followed by Burrows et al. (2011). We grouped data from neighboring epochs until the total counts exceeded 3000 and summed spectra using the `ftool sumpha`. The corresponding response files, i.e., the RMFs (Response Matrix Files) and the ARFs (Ancillary Response Files) were weighed as per ASASSN-14li’s counts in the individual epochs and combined using the tasks `addrmf` and `addarf`, respectively. This procedure translated to combining anywhere between a few to a few tens of neighboring observations. We then fit these averaged X-ray spectra (0.3–1.0 keV) separately with a blackbody model defined as `phabs*zashift(phabs*bbbodyrad)` in XSPEC (Arnaud 1996). The best-fit model parameters are listed in Table 1. It is evident that the temperature changes were modest during the first 180 days. This is consistent with Fig. 3 of Miller et al. (2015) and more recently with Fig. 5 of Brown et al. (2017).

To obtain the blackbody parameters in each epoch, we modeled the individual XRT spectra with the same blackbody model, but fixed the disk temperature and the absorbing column to lie within the error bars of the values of the nearest (in time) averaged spectrum. However, not all individual observations had enough counts to extract an X-ray spectrum. In these cases we assumed that their X-ray spectra have the same shape as that of the

³ <http://www.swift.ac.uk/analysis/xrt/pileup.php>

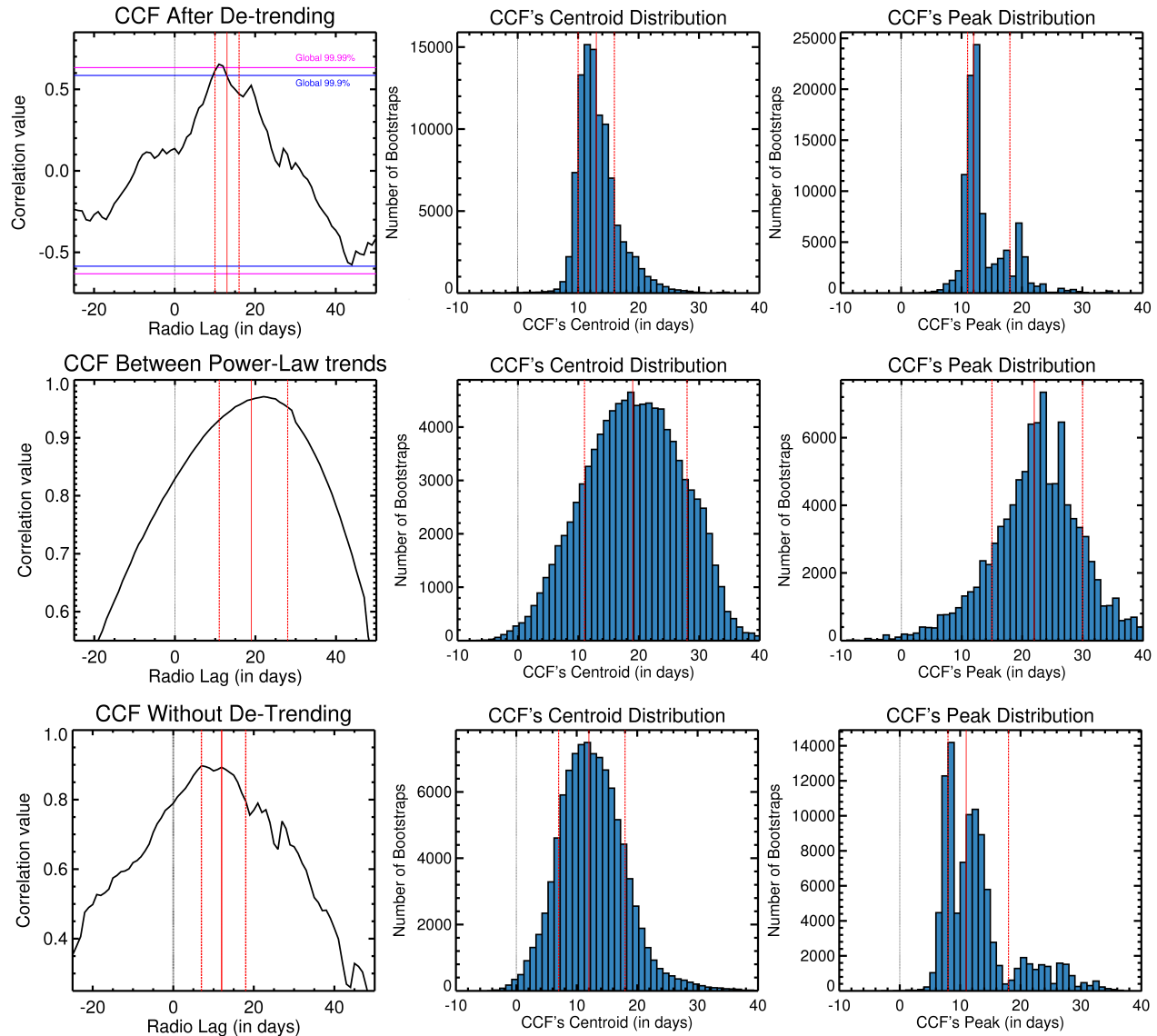


FIG. 2.— X-ray and radio cross-correlation functions (left) and corresponding centroid (middle) and peak (right) distributions. The top row panels correspond to CCF analysis after de-trending the X-ray and radio light curves. The middle row corresponds to the CCF plots between the best-fit power-law trends of the X-ray and radio light curves. The bottom row shows the CCF plots without de-trending the light curves. *The time lag between the X-ray and the radio is evident in all the three cases.* The horizontal blue and magenta lines in the top-left panel are the global 99.9% and the 99.99% white noise statistical confidence contours for a search between -25 and 50 days (see Sec. 3.2). The centroid and the peak distributions of each CCF are shown in the middle and right panels, respectively. These show the uncertainty in the centroid and the peak of the X-ray-radio lag after taking into account both the measurement and the sampling uncertainties of the light curves. The red dashed vertical lines in these two panels indicate the 1- σ deviation away from the median values (solid red lines). The centroids of the CCFs from top to bottom are 13^{+3}_{-3} , 19^{+9}_{-8} , and 12^{+6}_{-5} days, respectively.

observation closest in time to them. Fluxes in these low-count (<100) epochs were then estimated by scaling the flux of the nearest observation by the ratio of the PSF-corrected count rates. The 0.3-1.0 keV fluxes estimated from this approach are listed in Table A1.

For each XRT pointing we also extracted a mean source count rate corrected for the background, the exposure and vignetting using the `ftool xrtlccorr`. PSF correction was also performed by setting the keyword `psfflag = yes`. Exposure maps were also extracted to account for bad pixels. The resulting source count rates are shown in Table A1.

3. TIMING/CROSS-CORRELATION ANALYSIS

We computed the interpolated cross-correlation function (ICCF; see Gaskell & Peterson 1987; White & Peterson 1994; Peterson et al. 2004 and the references therein) between the 15.7 GHz radio and the X-ray light curves. As explained in Sec. 2.1), we subtracted the non-transient emission at 15.7 GHz, but we stress that the observed correlation and the lag (below) are independent of the value of the baseline flux.

Welsh (1999) argued that long-term trends in the light curves can sometimes bias the ICCF analysis and thus

de-trending⁴ with a smooth function can improve the ability to recover the correlation and the lag between the two time series under consideration. Therefore, we first de-trended both the X-ray and the radio light curves with a power-law decay model. The two light curves along with their best-fit decay model of the form $A \times (t - t_0)^{-\alpha}$ (where A , t_0 , and α are the model parameters, and t is the time in days) are shown in Fig. 1 (left and middle panels). The best-fit index value, α , and the $\chi^2/\text{degrees of freedom}$ for the X-ray light curve are 2.5 ± 2.4 and $127/46$, respectively. For the radio the corresponding values are 1.9 ± 0.1 and $62/27$, respectively. It should be noted that the purpose of modeling here is to only make an estimate of the long-term trend. Moreover, the index value and the time at peak (t_0) are degenerate (but see Sec. 4.4 where we estimate t_0 by modeling the evolution of radio spectra). The ICCF was then computed between the residual light curves (data minus the best-fit model). We also experimented with other de-trending models, viz., a linear model, and a second order polynomial model. The ICCFs in all these cases showed clear evidence for a radio lag around 13 days. Because of the theoretical expectation that the bolometric TDF light curves should decay as a power-law (Rees 1988; Lodato et al. 2009), which is consistent with most X-ray observations (Komossa 2002), we adopted the analysis corresponding to the power-law decay model. In contrast, P+17 used a bending-powerlaw model, but we stress that the cross-correlation between the X-ray and radio light curves is independent of the de-trending model (See Fig. 2). We computed the ICCFs using the steps outlined in P+17 (left panels of Fig. 2).

3.1. Visually assessing the cross-correlation

To allow a visual assessment of the strength of the cross-correlation, we placed the X-ray and radio light curve on top of each other (Fig. 1, right panel). We first displaced the observed X-ray light curve by 13 d, the median of the ICCF’s centroid (see Sec. 3.3). We then interpolated the X-ray light curve onto the time values of the radio data. The interpolated X-ray light curve (magenta) is overlaid on the 15.7 GHz radio data (blue) in the right panel of Fig. 1. It is clear that they both exhibit the same variability features. The black curves are a running mean of the data points in a 10 d window. Adapting the procedure outlined by Romero-Cañizales et al. (2011) we also extracted the 3σ variability contours. These are shown as dashed horizontal lines in the right panel of Fig. 1.

3.2. Statistical Significance Contours

The X-ray–radio ICCF in Fig. 2 clearly shows a peak centered around 13 d⁵. To assess the statistical significance of this peak, we estimated the global 99.9% and 99.99% Gaussian white noise confidence contours as follows. First, we extracted M values from a Gaussian distribution with a mean of zero and a standard deviation equal to the standard deviation of the observed de-trended X-ray light curve. Here, M is the number of data

⁴ De-trending refers to removing the long-term trend from the light curves.

⁵ The notation throughout the paper is such that a positive lag in the ICCF implies that the radio lags behind the X-rays.

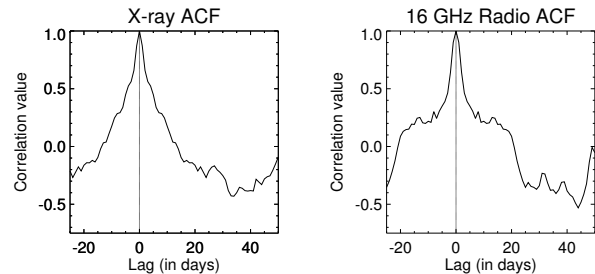


FIG. 3.— X-ray and radio auto-correlation functions (ACFs). The ACF of the X-ray and the radio light curves are shown in the left and the right panels, respectively. Both are obtained using the same CCF parameters as in Fig. 2. The difference in the two ACF shapes is only an artifact of the difference in the sampling of their respective light curves (see Sec. 3.6).

points in the observed X-ray light curve. By assigning these M values to be the flux values at the times of the observed X-ray light curve, we constructed a synthetic de-trended X-ray light curve sampled exactly as the observed X-ray light curve. This synthetic X-ray light curve was then cross-correlated with the de-trended radio light curve exactly as the observed ICCF. This procedure was repeated 10^6 times to construct 10^6 synthetic CCFs. We then constructed a distribution of all CCF values between -25 and 50 d. From this distribution we extracted the global 99.9 and 99.99% significance levels (see the left panel of Fig. 2).

3.3. Uncertainty on the Lag’s Centroid and Peak

We extracted the errorbars on the peak and the centroid lag values using the Flux Randomization (FR) and the Random Subset Selection (RSS) methods as described in Peterson (2004). These account for the measurement and the sampling uncertainties of both the light curves. We estimated the distribution of the centroid (top-middle panel of Fig. 2) and the peak (top-right panel) of the ICCF. The centroid was estimated using all correlation values greater than 0.8 times the peak.

Finally, we also repeated the entire cross-correlation analysis with the X-ray count rate light curve (instead of flux) and the resulting ICCF is consistent with the ICCF of the X-ray flux versus the radio flux. This is not surprising as the X-ray spectral changes were only modest (see Table 1) and therefore count rate serves as a good indicator of the flux.

3.4. Time Lag between the X-ray and Radio Trends

We also extracted an ICCF between the best-fit power-law trends of the X-ray and the 15.7 GHz radio light curves. These trends are indicated as red dashed curves in the left and middle panels of Fig. 1. Because the highest cross-correlation power in these trends is at the lowest frequency, one might expect the CCF of these two declining light curves to simply peak at zero lag. Instead, we find that the strongest cross-correlation value is at a finite lag (see Fig. 2). The best-fit lag centroid value is 19^{+9}_{-8} d and is consistent with the lag obtained from only the short-time scale fluctuations of the light curves, i.e., the CCF of the de-trended light curves (top panels of Fig. 2). This strongly suggests that not only are the variations in the radio and the X-rays are correlated but

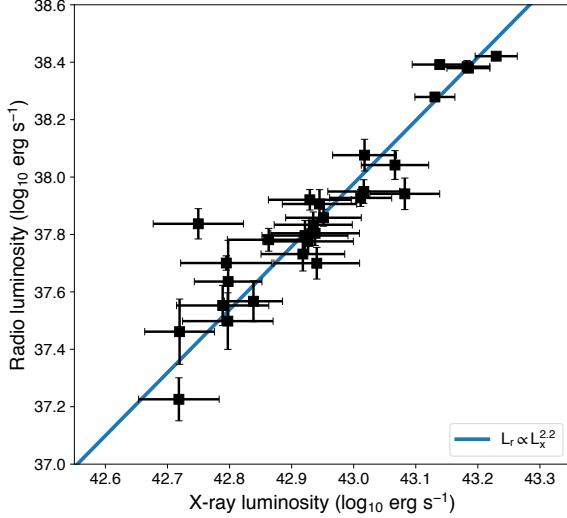


FIG. 4.— X-ray and radio luminosity. Here we show the lead-corrected X-ray luminosity and the 16 GHz radio luminosity (combining both the AMI and the VLA observations, both with the non-transient flux subtracted). The correlation between the luminosity in these two wavelengths can be described as $L_{\text{radio}} \propto L_{\text{X-ray}}^{2.2}$. The reduced χ^2 of the best-fit power-law relation is 0.6. This index suggests that the accretion and jet power of ASASSN-14li are linearly coupled (see Sec. 4.4).

the entire radio-emitting region is regulated by the X-ray engine.

3.5. CCF without de-trending

Finally, to establish that de-trending is not causing the correlation and the time lag, we also extracted an ICCF and its corresponding centroid and peak distributions between the observed 15.7 GHz radio and soft X-ray fluxes. These are shown in the bottom panels of Fig. 2. As expected the correlation and the lag are evident. In addition to ruling out any de-trending related artifacts this establishes that the entire radio and soft X-ray flux of ASASSN-14li are correlated with each other.

3.6. Auto-correlation Functions

A cross-correlation function is a convolution of the auto-correlation function (ACF) with the transfer function. A lag is real only if it originates from the transfer function and not from the ACF itself. To ensure that the lag seen in Fig. 2 did not originate from either of the X-ray or the radio ACF we evaluated both and show them in Fig. 3. Clearly, both the ACFs are centered on zero lag and thus assert that the observed lag originates from the transfer function.

The difference in the shapes of the two ACFs is due to the different sampling of the two light curves. Whether the X-ray light curve is lead-corrected and interpolated onto the radio epochs or vice versa, the resulting ACFs are similar (which is expected for two light curves that are highly correlated).

3.7. Correlation between X-ray and Radio Luminosity

After correcting for the lag between the X-ray and the radio light curves, we compared the contemporaneous luminosities at these two frequencies. Since the X-ray data are sampled with a higher cadence, we interpolated the

X-ray light curve onto the time stamps of the radio data. Following the “Nuker method” (Tremaine et al. 2002), we fit a power-law to the X-ray versus radio luminosity by minimizing the following merit function:

$$\chi^2(t_{\text{lag}}) = \sum \frac{(L_{\text{radio}}(t) + a - bL_{\text{X-ray}}(t + t_{\text{lag}}))^2}{\sigma_{\text{radio}}^2 + b^2\sigma_{\text{X-ray}}^2} \quad (2)$$

Here b is the X-ray–radio power-law index and a is the normalization; $L_{\text{X-ray}}(t)$ and $L_{\text{radio}}(t)$ denote the logarithms of the X-ray and the radio luminosity, respectively, as a function of time. $\sigma_{\text{X-ray}}$ and σ_{radio} are the logarithms of the X-ray and radio measurement uncertainties, respectively. The X-ray light curve is interpolated to a time $t + t_{\text{lag}}$, with t_{lag} being the observed CCF lag. We can estimate the statistical uncertainty on the best-fit power-law index under the assumption that Eq. 2 follows χ^2 statistics (Tremaine et al. 2002). To estimate the systematic uncertainty on the power-law index, we sampled the observed distribution of lags (Fig. 2, bottom middle panel) and obtained a distribution of best-fit values of b .

We find the following best-fit power-law index $b = 2.2 \pm 0.2$ (statistical) ± 0.3 (systematic), with a reduced χ^2 of 0.6. The data and this power-law relation are shown in Fig. 4. If no lag is applied to the X-ray light curve, the scatter in the luminosity–luminosity relation is significantly larger and the reduced χ^2 of the best-fit power-law is 2.0. An interpretation of the X-ray–radio luminosity relation is presented in Sec. 4.4.

4. SPECTRAL/SYNCHROTRON ANALYSIS

4.1. Evolution of the Peak Frequency

Using the formulae of synchrotron emission and self-absorption (e.g., Pacholczyk 1970) and an electron energy (E_e) distribution that follows a power law ($N_e dE_e \propto E_e^{-p} dE_e$), Marscher & Gear (1985) derived the dependence of the peak radio flux (S_{peak}) on the frequency at peak (ν_{peak}) for an adiabatically expanding region in a conical jet to be,

$$S_{\text{peak}} \propto \nu_{\text{peak}}^{\frac{10(p-1)}{7p+8}} \quad (3)$$

The above equation (Eq. 20, in Marscher & Gear 1985) assumes that the magnetic field strength (B) scales with the radius, r , (perpendicular to the jet axis) as $B \propto r^{-1}$ which is the case for a conical jet (Readhead et al. 1978; Falcke & Biermann 1995). Using an electron power-law index (p) between 2 and 3, the above equation then translates to

$$S_{\text{peak}} \propto \nu_{\text{peak}}^{0.57 \pm 0.12} \quad (4)$$

On the other hand, the peak synchrotron flux of a cloud that is expanding radially is given by Eq. 17b of van der Laan (1966):

$$S_{\text{peak}} \propto \nu_{\text{peak}}^{\frac{7p+3}{4p+6}}, \quad (5)$$

or, for $2 < p < 3$,

$$S_{\text{peak}} \propto \nu_{\text{peak}}^{1.27 \pm 0.06} \quad (6)$$

The difference in the two cases is due to the scaling of the magnetic field and the particle energy with radius.

For an adiabatically expanding blob in a conical jet geometry, the energy of a relativistic electron (E) falls off with radius as $E \propto r^{-2/3}$ (see Marscher 1980), while for a cloud of electrons that is adiabatically expanding in a spherical geometry, we have $E \propto r^{-1}$ (see van der Laan 1966)⁶.

Eqs. 4 and 6 can be compared to the observed evolution of ASASSN-14li’s radio SED to discriminate between an expanding jet and an expanding spherical cloud. Alexander et al. (2016) modeled each radio SED with a single volume that is in equipartition. Using their values of the peak flux and frequency we find $S_{\text{peak}} \propto \nu_{\text{peak}}^{0.61 \pm 0.04}$.

In order to extract the peak flux and the frequency at peak in a model-independent way, we fit the radio SEDs with a simple bending power-law function of the form:

$$S_\nu = \frac{S_0 \nu^{-\alpha_1}}{1 + \left(\frac{\nu}{\nu_{\text{bend}}}\right)^{(\alpha_2 - \alpha_1)}} \quad (7)$$

Here, S_0 and ν_{bend} are the normalization and the frequency at which the SED turns over, respectively. α_1 and α_2 are the spectral index for frequencies (ν) much smaller than and much larger than ν_{bend} , respectively. We fixed the low-frequency slope (α_1) to be equal to the value for synchrotron self-absorption ($\alpha_1 = -2.5$). Using the five of the best sampled SEDs from Alexander et al. (2016), i.e., those taken on 2015 Jan 6/13, 2015 Mar 13, 2015 April 21/22, 2015 June 16/21 and 2015 Aug 28/Sept 8/11, we find that the observed peak flux ($S_{\text{peak,obs}}$) and the frequency at peak ($\nu_{\text{peak,obs}}$) evolve as

$$S_{\text{peak,obs}} \propto \nu_{\text{peak,obs}}^{0.46 \pm 0.1} \quad (8)$$

This observed scaling disfavors a uniformly expanding single spherical cloud model and is consistent with the bulk of the radio emission originating from a conical geometry that is adiabatically expanding, see Fig. 5.

4.2. Single-zone Models

Consider a spherical region of radius R that is uniformly filled with magnetic fields (B) and relativistic electrons with an energy distribution $N_e d\gamma_e = K \gamma_e^{-p} d\gamma_e$, where γ_e and K are the electron Lorentz factor and the normalization, respectively. When observed at a distance D , the observed synchrotron flux of this region is given by

$$S_\nu = \delta^2 \frac{R^2}{4D^2} \frac{\epsilon_{\nu'}}{\kappa_{\nu'}} (1 - e^{-\kappa_{\nu'} R}) \quad (9)$$

Here δ is the Doppler factor of the region, and ν is the observed frequency. The synchrotron absorption ($\kappa_{\nu'}$) and emission ($\epsilon_{\nu'}$) coefficients depend on the magnetic field, the electron energy distribution, and the frequency

⁶ The scaling of the particle energy with source radius can be derived from the ideal gas equation for relativistic particles as follows. The ideal gas equation of state for relativistic particles is $Pr \propto n_e^{4/3}$, where Pr and n_e are the pressure and the electron density in the gas, respectively. We have $Pr = n_e \langle E \rangle$, where $\langle E \rangle$ is the mean energy of an electron in the gas, hence $\langle E \rangle \propto n_e^{1/3}$. For a spherical cloud of relativistic electron gas, the electron density falls off with radius as $n_e \propto r^{-3}$. Thus $\langle E \rangle \propto r^{-1}$ for a spherical geometry. However, for an expanding jet, $n_e \propto r^{-2}$ and thus $\langle E \rangle \propto r^{-2/3}$.

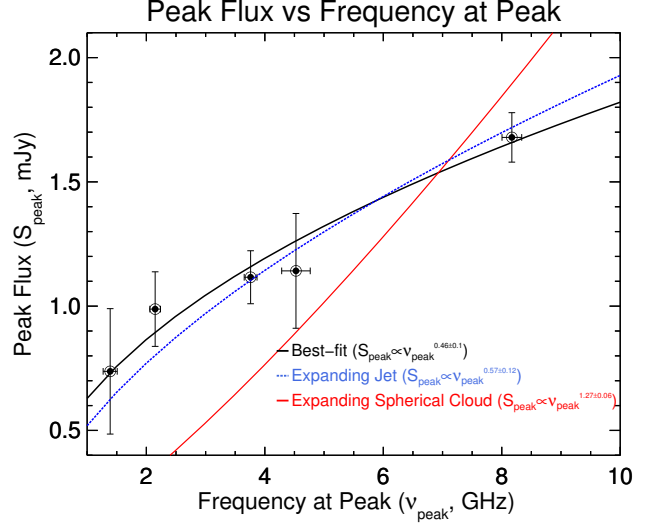


FIG. 5.— Radio SED evolution: conical jet compared to a spherical cloud. Evolution of the peak radio flux vs. the frequency at peak (black data points). The best-fit power-law index of 0.46 ± 0.1 is shown by a solid black curve while the index for an adiabatically expanding jet (Marscher 1980) and an adiabatically expanding spherical cloud (van der Laan 1966) are shown by the dashed blue and the red curves, respectively.

in the rest-frame of the jet, $\nu' = \nu/\delta$. We solve for the normalization of these coefficients by assuming equipartition between the energy in the electrons and the magnetic field, $B^2/8\pi = \int N_e d\gamma_e$. Equipartition implies a minimum in the total energy of the system (i.e., the sum of the energy in the magnetic field and the synchrotron-emitting particles). Observations of the lobes of radio galaxies (Croston et al. 2005; Kataoka & Stawarz 2005; Harwood et al. 2016) as well as AGN jets (Burbidge 1956; Readhead et al. 1978; Herrnstein et al. 1997; Falcke et al. 1999) provide strong evidence that equipartition is commonly reached for these sources. We confirmed that for $\gamma_{\text{max}} \gg \gamma_{\text{min}}$, our implementation of the synchrotron formalism (Eq. 9) gives the same results as the fitting formula for synchrotron emission given in Chevalier (1998).

As expected based on earlier work (Alexander et al. 2016; Krolik et al. 2016), we find that the synchrotron emission from a single region (Eq. 9) provides a reasonable fit to the radio SEDs of ASASSN-14li. For this fit we adopted $\gamma_{\text{min}} = 1$, $p = 2.2$ and $\gamma_{\text{max}} = 10^4$, but we stress that the resulting magnetic field and radius are only weakly dependent on these assumptions. For $\delta = 1$ (i.e., a non-relativistic outflow), this single-zone synchrotron model yields $B \approx 0.1$ G and $r \approx 4 \times 10^{16}$ cm for the observations of April 2015. For this magnetic field, the synchrotron cooling time at 10 GHz is ~ 10 yr, which supports the assumption that $\gamma_{\text{max}} \gg \gamma_{\text{min}}$. For this single-zone model, we find that the equipartition magnetic field scales with source size as $B \propto R^{-1.2}$.

The hotspots or the forward shock of a jet or outflow can be modeled using a single-zone equipartition model. However, establishing the observed cross-correlation in a single-zone model proves to be very difficult. First of all, the light crossing time of this region grows from ≈ 10 d to ≈ 30 d during the period of the 15.7 GHz monitoring observations, thus exceeding the duration of the cross-correlation lag. A second problem of establishing an X-

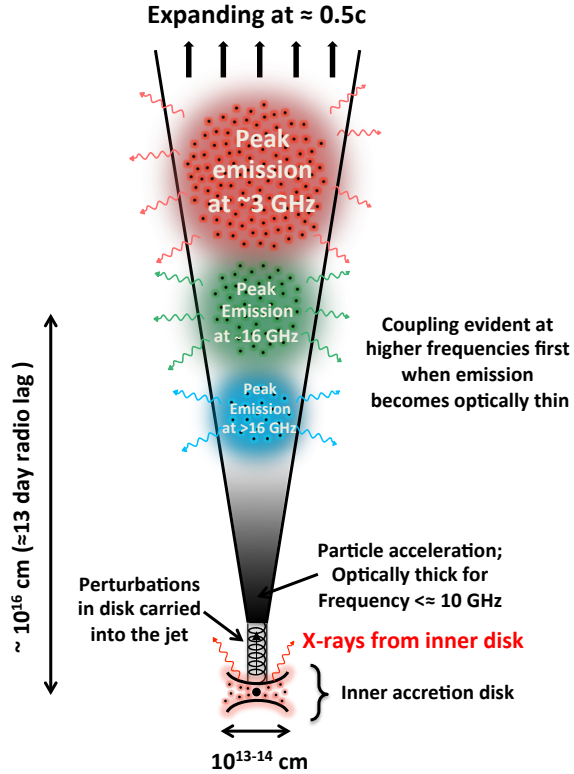


FIG. 6.— Schematic of the proposed jet model for the tidal disruption flare ASASSN-14li. Shown here is a snapshot of the jet at the end of the radio monitoring observations (June, 2015). The X-ray–radio correlation and the radio spectral evolution can both be explained as follows. First, perturbations in the accretion rate are manifested as X-ray flux variations and, via the disk–jet coupling, lead to perturbations in the jet power. The jet power is used to accelerate electrons, which produce synchrotron emission. As the synchrotron radiating electrons are swept further along the jet axis, they start to cool adiabatically. When their emission becomes optically thin to self-absorption at 15.7 GHz, at $\sim 10^{16}$ cm from the black hole (about 13 d later), the observed X-ray–radio correlation emerges. Applying our jet model to the radio observations of ASASSN-14li (Fig. 7), we estimate the jet flow velocity at these radii to be about $0.5c$.

ray–radio correlation within a single region is the long synchrotron cooling time at 16 GHz (~ 10 yr). Over the course of the 16 GHz monitoring observations (≈ 180 d), the region cannot radiate the energy it has received and thus the relative amplitude of fluctuations in the radio light curve due to fluctuations in the X-ray light curve should decrease with time.

To summarize, while a single-zone equipartition model for ASASSN-14li can reproduce the observed radio SEDs, its size is likely to be too large to produce variability on a 10 d timescale. Moreover, due to the long synchrotron cooling time, the addition of new energy to has a negligible effect on the radio flux. This leads us to consider a freely expanding jet as the source of the observed radio emission.

4.3. Adiabatic Jet Model

A conical equipartition jet model is widely used to explain the properties of compact radio cores of AGN and X-ray binaries (Blandford & Königl 1979; Falcke & Biermann 1995; Falcke et al. 1995; Crumley et al. 2017). In this model, electron acceleration happens internal to the

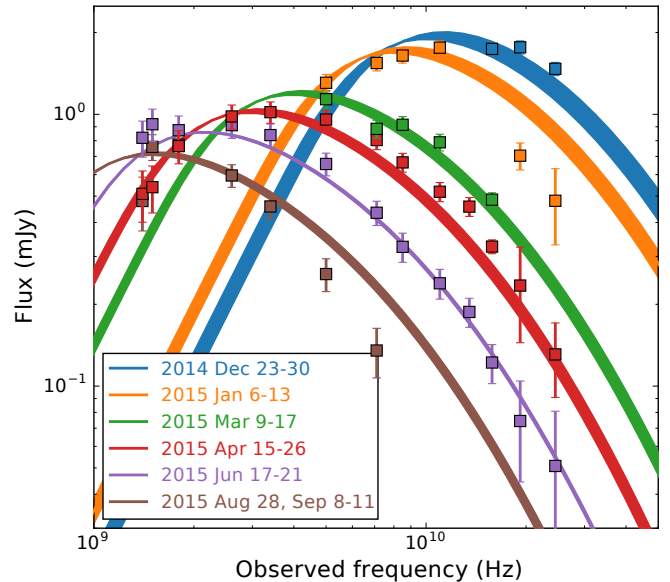


FIG. 7.— Adiabatic jet model and multi-frequency radio observations of ASASSN-14li. This jet model is a superposition of synchrotron-emitting spheres, each expanding with the same velocity in a conical jet geometry. The electrons in each region in the jet cool adiabatically, which yields the decrease of the peak luminosity with time. Data points with the same colors are semi-simultaneous (epochs are labeled in the legend). The width of each model curve indicates the range of the predicted flux due to the temporal spread of the observations.

jet (e.g., via collimation shocks) and equipartition is established at each radius in the jet that lies beyond the nozzle where the jet is accelerated.

Summing the optically thin synchrotron emission in the model for AGN jet cores yields the characteristic flat spectrum, $S_\nu \propto \nu^0$. However, the peak of the radio SED of ASASSN-14li decreases with time, $S_{\text{peak}} \propto \nu_{\text{peak}}^{0.5} \propto t^{-0.5}$. This suggests that we are observing the adiabatic evolution of electrons that have been heated prior to becoming optically thin to synchrotron self-absorption (Marscher & Gear 1985). Besides the evolution of the peak frequency (see Sec. 4.1), additional evidence for this adiabatic evolution is the apparent exponential turnover at $\nu \approx 15$ GHz in the radio SEDs (see Fig. 7). This turnover is most clearly seen in the radio data taken on 2015 Aug 28, Sep 8–11 (see Fig. 7). While this can be explained by synchrotron cooling, matching the cooling time at 16 GHz to the dynamical time requires a magnetic field that is two orders of magnitude higher than the observed equipartition value. In other words, the observed high-frequency break in the radio spectra can be explained by synchrotron cooling, but only if the particles were accelerated in a region with a magnetic field that is higher than the equipartition value. This can be established if the acceleration happened downstream in a jet (i.e., closer to the black hole), where the magnetic strength is larger. To include the effect of synchrotron cooling on the spectral shape, we allow the maximum Lorentz factor of the electrons, γ_{max} , to be a free parameter in our jet model.

To predict the light curve in an adiabatic jet model, we use a superposition of non-overlapping spheres in a

TABLE 2
BEST-FIT PARAMETERS OF AN ADIABATIC JET MODEL.

Relevant equation	Free parameters	$\phi = 1/5$	$\phi = 1/10$	$\phi = 1/15$ d
$B(z) = B_0(z/10^{15}\text{cm})^{c_B}$	B_0 (G)	9.6 (2.3)	7.6 (2.0)	8.0 (2.0)
	c_B	−1.02 (0.06)	−1.02 (0.05)	−1.07 (0.05)
$Q_{\text{jet}} \propto (z/z_{\text{head}})^{c_Q}$	c_Q	1.20 (0.4)	1.20 (0.4)	1.40 (0.2)
	$\log_{10} \gamma_{\text{max}}$	1.9 (0.4)	2.0 (0.3)	2.0 (0.2)
$z_{\text{jet}}(t) = v_{\text{jet}}(t - t_0)$	t_0 (MJD + 56887)	63 (11)	64 (11)	48 (12)
	v_{jet} (c)	0.37 (0.1)	0.62 (0.2)	0.71 (0.2)
Inferred parameters				
$\tau(16\text{ GHz}) = \kappa z_{16} = 1$	z_{16} ($\times 10^{16}$ cm)	$3.3^{+2.1}_{-2.0}$	$3.4^{+3.9}_{-1.6}$	$1.5^{+2.8}_{-1.2}$
$v_{\text{lag}} = (c \tau_{\text{lag}}/z_{16} + \cos i)^{-1}/\gamma$	v_{lag} (c)	$0.6^{+0.3}_{-0.2}$	$0.6^{+0.3}_{-0.2}$	$0.3^{+0.3}_{-0.2}$

NOTE. — The first six rows of the second column list the parameters of our jet model, with the relevant equations listed in the first column (see Sec. 4 for details). Their best-fit values (including 1σ uncertainties) are listed in the third to last columns, for three different values of the jet opening angle (ϕ). We can use the best-fit parameters to infer the radius where the jet becomes optically thin to self-absorption at 16 GHz (z_{16}). Using the observed lag between the radio and the x-ray light curves (τ_{lag}) we can compute the mean communication velocity (v_{lag}) between the black hole accretion disk and the 16 GHz self-absorption radius. We find that this estimate of the disk-jet communication velocity is consistent with the best-fit jet velocity (v_{jet}). All parameters listed here are estimated after adopting a jet inclination of $i = 60^\circ$.

conical geometry (Fig. 6), each with a flux given by their magnetic field and radius (Eq. 9). If each sphere receives the same amount of jet power, the total flux (i.e., the contribution from all the spheres) yields the well-known flat spectrum, $S_\nu \propto \nu^0$. Following van der Laan (1966) and Marscher & Gear (1985) we account for adiabatic cooling of electrons via the normalization of the electron energy distribution

$$K(z > z_0) = (z/z_0)^{2(1-p)/3}. \quad (10)$$

Here z is the distance measured along the jet axis and z_0 is the distance from the black hole where electrons are no longer accelerated and the jet starts to cool. Adding this cooling term to Eq. 9, we retrieve the scaling of Marscher & Gear (1985) for the peak flux with frequency at peak of an adiabatic jet (Eq. 3).

Since we have a rapid decrease in the accretion power, we expect that the jet power (Q_j) downstream from the jet head (z_{head}) will decrease. We model this with a power-law scaling,

$$Q_j(z, t) = (z/z_{\text{head}}(t))^{c_Q}, \quad (11)$$

with c_Q a free parameter. A second free parameter of our jet model is the scaling of the magnetic field along the jet axis

$$B(z, t) = B_0(z/z_0)^{c_B} \times Q_j^{1/2}(z, t). \quad (12)$$

If no magnetic energy is lost and the jet can freely expand to yield a conical geometry we expect $c_B = -1$ (Blandford & Rees 1974; Blandford & Königl 1979; Falcke & Biermann 1995). We stress that c_B and c_Q are not degenerate; c_B parameterizes how the radio flux from every regions in the jet changes as it expands while c_Q determines how the jet power scales relative to the peak jet power carried by the jet head.

The next two free parameters of our model concern the jet dynamics. Motivated by the inference that a linear growth provides a good description of the equipartition

radius as a function of time in a single-zone synchrotron model (Alexander et al. 2016; Krolik et al. 2016), we assume a linear growth of jet head with time

$$z_{\text{head}}(t) = v_{\text{jet}} \delta(t - t_0), \quad (13)$$

with v_{jet} the rest-frame jet velocity and t is measured in the observer frame.

The last two free parameters in our model are the jet opening angle, $\phi = r/z$, and the inclination, i . When the inclination is known, the Doppler factor can be computed using the jet velocity, $\delta = 1/(\gamma_{\text{jet}}(1 - \beta_{\text{jet}} \cos i))$. We also compute the emission from the counter jet, observed at $i - \pi$, but its contribution is sub-dominant for most inclinations.

Eqs. 9–13 together yield our jet model. This model has nine free parameters, (v_{jet} , t_0 , B_0 , z_0 , c_Q , c_B , γ_{max} , ϕ , and i), compared to the 82 observations of the radio flux (the combination of the WSRT, AMI, and VLA data). For comparison, determining the velocity in a single-zone equipartition model requires six parameters: v , t_0 , B_0 , i , γ_{max} , plus a factor to account for the geometry of the emitting region.

If no adiabatic cooling is included, z_0 is simply a normalization constant with no physical meaning, i.e., it can be set to any value. However, when cooling is included (Eq. 10), z_0 can be thought of as the distance from the black hole where adiabatic cooling becomes important. We set $z_0 = 10^{15}$ cm, but we stress that this choice has no effect on the inferred jet dynamics or magnetic field scaling along the jet axis. When adiabatic cooling starts, the jet internal energy scales as $z^{-8/3}$ (Crumley et al. 2017). Hence for our choice of z_0 , the jet has lost a factor ~ 10 of its energy by the time of the first radio observations. (In principle, z_0 can be constrained if we include a self-consistent treatment of synchrotron cooling in our jet model; while this is beyond the scope of this work, we do note that $z_0 \ll 10^{15}$ cm can be ruled-out since this yields a γ_{max} that is too low to explain the observed radio SEDs).

We fixed the jet inclination at its a priori most-likely value, $i = 60^\circ$, but we will explore less probable inclinations below. Finally, the opening angle of the jet is poorly constrained by the radio observations alone. To allow the new jet to be freely expanding, it likely has to remain within the volume swept clear by the jet that was active prior to the tidal disruption. We therefore adopt $\phi = 1/10$ as a fiducial value and also consider the best-fit jet parameters for larger/smaller opening angles.

In our fit for the parameter of the adiabatic jet model, we enforced a 5% minimum statistical uncertainty on the radio data. This avoids putting too much weight on the early VLA observations, where the statistical uncertainty almost certainly exceeds the variance due to the limitations of our simple model. To subtract the non-transient radio flux, we use Eq. 1. If we instead adopt the non-transient flux that was used in the analysis of Alexander et al. (2016), we infer similar values for the free parameters of our model.

We use a least-squares fit to estimate the parameters of our jet model; the results are summarized in Table 2. The reduced χ^2 of the best fit is 3.6. To approximately include the variance due to the limitations of our model into the derived parameters, we multiplied the statistical uncertainty of the best-fit parameters by $\sqrt{3.6}$.

We find that the inferred jet velocity depends on the assumed opening angle, for $1/15 < \phi < 1/5$ we obtain $0.3 < v_{\text{jet}}/c < 0.7$. The inferred values of the other parameters are essentially independent on the opening angle. Since the jet Lorentz factor is modest, the effect on the jet inclination on the best-fit parameters is relatively small (e.g., for $\phi = 1/10$ and $i = 90^\circ$, $v_{\text{jet}} = 0.6c$, while the same jet opening angle observed at $i = 0$ yields $v_{\text{jet}} = 0.5c$). We find that 80% of the total jet flux is reached when the first four synchrotron-emitting spheres are summed, with the first sphere (i.e., the jet head) contributing about 30% of the total flux.

The power-law index that sets the scaling of the magnetic field strength along the jet axis is a free parameter in our model. We find $c_B = -1.02 \pm 0.03$, in excellent agreement with the expected $B \propto z^{-1}$ scaling for a conical jet geometry and conservation of magnetic energy (Blandford & Königl 1979; Falcke & Biermann 1995). By extrapolating to $z = 0$, we estimate that the jet was launched near the second week of June, 2014.

When the magnetic field is known, our jet model can be used to estimate the optical depth of each zone in the jet. Since the cross-correlation can only be observed when the synchrotron emission is optically thin, our prediction for the radius where $\tau = 1$ at 16 GHz provides a consistency check on our jet model. This radius yields an estimate of the communication velocity between the disk and the region from where the majority of the 16 GHz flux originates. The communication velocity can be estimated as $v_{\text{lag}}/c = \gamma^{-1}(\eta_{\text{lag}}c/z_{\text{lag}} + \cos(i))^{-1}$, with η_{lag} the observed delay between the X-ray and the radio light curves. Using our best-fit value for the magnetic field at MJD=57018 (which corresponds to the peak of the first correlated feature in the two light curves, about one month into the 16 GHz monitoring campaign, see Fig. 1), this estimate of v_{lag} is consistent with jet velocity predicted by our model (see Table 2).

4.4. Coupling between Accretion Rate and Jet Power

Under the assumption of a constant expansion velocity, our estimate of the jet power scaling obtained in the previous subsection can be translated to a scaling of the jet power with time. Along the jet-axis, $Q_j \propto z^{1.2 \pm 0.4}$. Under the assumption of a constant expansion velocity, we thus obtain $Q_j \propto t^{-1.2 \pm 0.4}$. Interestingly, this relation is consistent with the slope of the observed X-ray flux decay, $L_{\text{X-ray}} \propto (t - t_0)^{-1.7 \pm 0.1}$ (here we fixed the time normalization, t_0 , to our estimate of the time when the jet was launched). This X-ray flux decay index is also close to the expected fallback rate of the stellar debris, $t^{-5/3}$ (Phinney 1989). Because the thermal X-ray energy spectrum suggests an efficient accretion disk we expect the X-ray luminosity to be proportional to the mass accretion rate, $L_{\text{X-ray}} \propto \dot{m}$ (e.g., see Fig. 1 of Sądowski et al. 2011; Abramowicz & Fragile 2013; Lodato & Rossi 2011). From the evolution of the radio spectral energy distribution we thus find evidence that the jet power decays in concert with the accretion rate.

A second piece of evidence for linear jet-disk coupling follows from the correlation between the X-ray and radio luminosity. Because in section 3 we concluded that entire radio flux is correlated with the X-rays (see Fig. 2) we can use this correlation to estimate the coupling strength between the mass accretion rate and the jet power (see also Bright et al. 2018).

Using Eq. (7) of Heinz & Sunyaev (2003) it can be seen that the optically thin synchrotron emissivity, j_ν , at a given radio frequency (ν) for a power-law distribution of electrons with index p is given as

$$j_\nu = J_p K B^{\frac{p+1}{2}} \nu^{-\frac{p-1}{2}} \quad (14)$$

where J_p is a constant weakly dependent on p , and B is the magnetic field strength, and K is defined as before (see 4.2).

Thus, at a given radio frequency

$$j_\nu \propto L_{\text{radio}} \propto K B^{\frac{p+1}{2}} \quad (15)$$

where L_{radio} is the radio luminosity at ν . The jet power scales with the magnetic field strength as $Q_j \propto B^2$ and, under the assumption of equipartition $K \propto B^2$. Combining these two relations, we find (Heinz & Sunyaev 2003, their Eq. 16)

$$L_{\text{radio}} \propto Q_j^{1+\frac{p+1}{4}} \quad (16)$$

For, $2 < p < 3$ the index is 1.875 ± 0.125 .

From the observed X-ray and radio luminosities, we have $L_{\text{radio}} \propto L_{\text{X-ray}}^{2.2 \pm 0.3}$. Combining these into Eq. 16 results in

$$Q_j \propto \dot{m}^{1.2 \pm 0.2} \quad (17)$$

We thus see that the accretion and the jet power follow a roughly linear coupling. A caveat is that Eq. 16 is valid for a single region in the jet. While the 16 GHz emission is dominated by the radius where the jet becomes optically thin to self-absorption, other regions also provide a sub-dominant contribution to the 16 GHz flux. Correcting for this requires a more complete jet model than the toy model used in this work.

5. DISCUSSION

Our main conclusions, in order, are as follows.

1. We detected a correlation, significant at greater than the 99.99% level, between the soft X-ray and the 15.7 GHz radio variability of the thermal TDF ASASSN-14li. The radio emission lags the X-rays by about 12 d (Fig. 2).
2. The cross-correlation is inconsistent with external emission models (i.e., shocks driven into the circumnuclear medium) since in such models the radio emission is expected to evolve independently of the accretion rate or fallback rate.
3. We propose that the electrons responsible for the observed synchrotron emission are accelerated inside a jet which provides a natural vehicle to couple the radio-emitting region with the X-ray emitting region (Fig. 6).
4. Emission from a cloud of electrons that is adiabatically expanding in a conical jet geometry provides a good match to the observed evolution of the radio SEDs (Figs. 5 & 7).
5. Our jet model correctly predicts the observed time lag between the radio and X-ray light curves.
6. The observed scaling between the X-ray and the 16 GHz radio flux (Fig. 4) suggests that the accretion and the jet power are roughly linearly coupled (see Sec. 4.4).
7. From our jet model we obtain the jet power as a function of radius (Table 2), again finding a scaling that is consistent with a linear disk–jet coupling (see Sec. 4.4).

Below we discuss a few implications of these conclusions. First, we discuss our results in context of P+17, followed by a comparison of ASASSN-14li to sources on the fundamental plane, and then briefly remark on the implications for jet physics.

5.1. Connection to the Optical/UV–X-ray cross-correlation

P+17 discovered that the bulk of the optical/UV emission from ASASSN-14li is produced roughly 32 d ahead of the X-rays. They suggested that energy and perturbations from debris stream self-interactions could produce optical/UV emission and their corresponding fluctuations, respectively. These are then carried down to the inner accretion region where they modulate the X-rays. Combining this with the radio lag reported here suggests that the optical/UV emission does not originate from the jet. In other words, radio does not originate from the same site as the optical/UV light.

The observation that the fluxes in a wide range of the electromagnetic spectrum are correlated with X-rays—and thus with each other—leads to the following account that ties together the multi-wavelength properties of ASASSN-14li. The UV/optical emission is produced first, at the location where the debris streams intersect. Matter then falls to the center to form a compact, X-ray

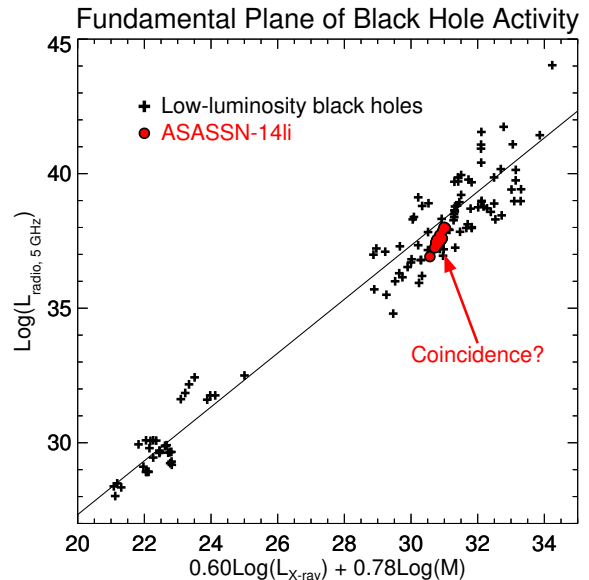


FIG. 8.— ASASSN-14li on the fundamental plane of black hole activity. The black data (crosses) show the fundamental plane of black hole activity as derived in Merloni et al. (2003) with their best-fit relation. Observations of ASASSN-14li data are shown in red (filled circles). $L_{X\text{-ray}}$, M , and $L_{\text{radio}, 5\text{GHz}}$ are the 2–10 keV X-ray luminosity, and the black hole mass in units of solar mass, and the 5 GHz radio luminosity, respectively. Because ASASSN-14li is a very soft X-ray source (Miller et al. 2015), its X-ray luminosity is estimated in the 0.3–1.0 keV energy range. Moreover, it should be cautioned that the 0.3–1.0 keV luminosity of ASASSN-14li only represents a small fraction of the accretion luminosity and is different from the typical 2–10 keV used for low-luminosity black holes.

emitting accretion disk. Perturbations to energy supply at the location of the optical/UV region are carried into the X-ray disk and ultimately show up as variability in the radio-emitting jet.

5.2. Comparison to AGN and X-ray Binary Jets

Black holes accreting at only a few percent of their Eddington limit are known to exhibit accretion–jet coupling (Merloni et al. 2003; Falcke et al. 2004; Gallo et al. 2003). For some supermassive black holes it has been possible to detect a time lag on the order of a few tens of days between the radio emission from the compact jet core and the hard X-ray (>2 keV) emission (Marscher et al. 2002; Bell et al. 2011; Chatterjee et al. 2011). These observations all point to a coupling between black hole jets and accretion disks.

Work by Merloni, Heinz, & di Matteo (2003) and Falcke, K rding, & Markoff (2004) has shown that for black holes in the “hard-state” (see Remillard & McClintock 2006 for a definition of this accretion state), the hard X-ray (2–10 keV) luminosity, the 5 GHz radio luminosity and the black hole mass are correlated, thus spanning a plane. This relation—the fundamental plane of black hole activity—extends all the way from stellar to supermassive black holes, ranging over roughly seven orders of magnitude in black hole mass (see Fig. 8).

To place ASASSN-14li on the fundamental plane of black hole activity, the 5 GHz radio luminosity was estimated at each 15.7 GHz epoch by interpolating the radio SEDs using our best-fit jet model. It is evident that the

soft X-ray luminosity and the 5 GHz radio luminosity of ASASSN-14li fall very close to the fundamental plane. Allowing the mass to vary in between 10^5 to $10^7 M_\odot$ the observations of ASASSN-14li do not move significantly away from the plane.

Our finding that the X-ray and radio properties of ASASSN-14li are consistent with the fundamental plane of black hole activity could be considered surprising. First of all, the slope of the X-ray–radio correlation of ASASSN-14li (2.2, Fig. 4) is much steeper than slope of the plane (0.6), at a fixed black hole mass. Furthermore, the X-ray emission from ASASSN-14li is thermal and soft (0.3–1 keV), thus likely originating from an radiatively efficient accretion flow (Abramowicz & Fragile 2013); the X-ray luminosity of sources on the fundamental plane is dominated by non-thermal emission (in the 2–10 keV band). These hard X-rays presumably originate from an X-ray corona rather than a radiatively efficient accretion disk. It has been suggested that the X-ray corona can either be an inefficient inner accretion flow (Yuan & Cui 2005) or the base of the jet, among other possibilities (Markoff et al. 2005). In either scenario, the X-ray emission site for these black holes is physically different from ASASSN-14li. The close match to the fundamental plane could simply be a coincidence, although we note that the 2–10 keV output of the powerful jetted TDF Swift J1644+57 is also consistent with the fundamental plane (Miller & Gültekin 2011).

5.3. A Jet Power Dichotomy?

A linear coupling between the jet power and accretion power is well-established for radio-loud quasars (Rawlings & Saunders 1991; Falcke et al. 1995; van Velzen et al. 2015). The hard X-ray light curve of the powerful jetted TDF Swift J1644+57 closely matches the power-law decay expected for the fallback rate of the stellar debris (Levan et al. 2016). Since the X-rays of this source almost certainly originate from the base of a relativistic jet (however see, Kara et al. 2016), these observations suggest that Swift J1644+57 may also displays a linear disk–jet coupling. Combining this with our discovery of a linear coupling between the accretion rate and the jet power for ASASSN-14li, may lead one to conclude that a similar jet engine operates for both radio-loud quasars and jets from TDFs such as ASASSN-14li and Swift J1644+57. However this unified picture is challenged by the difference in radio luminosity between these two TDFs.

The difference in the jet energy of Swift J1644+57 and the equipartition energy of ASASSN-14li is about 4 orders of magnitude (Alexander et al. 2017). Relativistic Doppler boosting is not a solution to explain this difference since the late-time radio emission of Swift J1644+57 is most likely isotropic (Mimica et al. 2015). We further note that the host galaxies of these events have a similar central black hole mass, $M \sim 10^6 M_\odot$, as inferred from the host galaxy properties (Levan et al. 2016; Wevers et al. 2017). Since our jet model for ASASSN-14li requires adiabatic cooling to explain the evolution of the SED, the true jet energy of this source is likely to be an order of magnitude higher than the equipartition energy inferred from the radio SED (see Sec. 4.3). However, to

be consistent with observed radio SED, the correction due to adiabatic cooling cannot be arbitrarily large. We thus conclude that the difference in isotropic jet power between Swift J1644+57 and ASASSN-14li is 2–3 orders of magnitude.

The difference in jet power could be explained by a difference in jet efficiency, i.e., the conversion of accretion power to jet power. Parameters that may affect this efficiency are black hole spin and the magnetic field near the horizon. Alternatively, to uphold a unified scenario in which all TDFs have a similar jet efficiency, the amount of accretion energy available for jet production must be higher for Swift J1644+57. This difference could be established by the orbit of the star. Consider a deeply plunging orbit (i.e., a pericenter much smaller than the tidal radius). These events likely yield rapid circularization, and thus accretion, of the stellar debris (Dai et al. 2015). The result is a longer super-Eddington accretion phase compared to stars that are disrupted close to the tidal radius. If the jet is powered only when the accretion rate is super-Eddington (e.g., Coughlin & Begelman 2014), deeply plunging tidal disruptions could thus yield more powerful jets.

While a freely expanding jet appears to provide the only self-consistent explanation for both the observed radio SEDs and the X-ray–radio correlation of ASASSN-14li, an uncomfortable feature of this model is the requirement of a low external particle density on a scale of 10^{16} cm from the black hole. This can be reconciled if the newly launched TDF jet propagates along the same axis as the jet that was operating during the AGN activity prior to the stellar disruption. Thermal TDFs by black holes that had no active jet prior to the disruption may therefore not produce month-long radio flares. This could explain the radio non-detection in a recent nearby TDF (Blagorodnova et al. 2017) where a radio flare similar to ASASSN-14li would have been detectable.

Acknowledgments: This work is based on observations made with *Swift*, a mission that is managed and controlled by NASA’s Goddard Space Flight Center (GSFC) in Greenbelt, Maryland, USA. The data used in the present article is publicly available through NASA’s *HEASARC* archive. We would like to thank Edo Berger, Bradley Cenko, Heino Falcke, Glennys Farrar, Rob Fender, Elmar K rding, Andrei Gruzinov, Jeroen Homan, Christian Knigge, Julian Krolik, Sara Markoff, Andrea Merloni, Giulia Milgari, James Miller-Jones, Gabriele Ponti, and especially Alan Marscher and Abdu Zoghbi for valuable discussions. We would like to thank the referee for detailed comments and suggestions that helped us improve the manuscript. Pasham is supported by NASA through an Einstein fellowship (PF6-170156) and van Velzen is supported by NASA through a Hubble Fellowship (HST-HF2-51350). All the data presented here is public and can be found in Table A1, van Velzen et al. (2016b), Alexander et al. (2016), and the NASA/*Swift* archive.

Facilities: AMI, VLA, Swift.

REFERENCES

- Abramowicz, M. A., & Fragile, P. C. 2013, *Living Reviews in Relativity*, 16, 1
- Alexander, K. D., Berger, E., Guillochon, J., Zauderer, B. A., & Williams, P. K. G. 2016, *ApJ*, 819, L25

- Alexander, K. D., Wieringa, M. H., Berger, E., Saxton, R. D., & Komossa, S. 2017, *ApJ*, 837, 153
- Arcavi, I., Gal-Yam, A., Sullivan, M., et al. 2014, *ApJ*, 793, 38
- Arnaud, K. A. 1996, in *Astronomical Society of the Pacific Conference Series*, Vol. 101, *Astronomical Data Analysis Software and Systems V*, ed. G. H. Jacoby & J. Barnes, 17
- Auchettl, K., Ramirez-Ruiz, E., & Guillochon, J. 2017, *ArXiv e-prints*, arXiv:1703.06141
- Bade, N., Komossa, S., & Dahlem, M. 1996, *A&A*, 309, L35
- Bell, M. E., Tzioumis, T., Uttley, P., et al. 2011, *MNRAS*, 411, 402
- Berger, E., Zauderer, A., Pooley, G. G., et al. 2012, *ApJ*, 748, 36
- Blagorodnova, N., Gezari, S., Hung, T., et al. 2017, *ArXiv:1703.00965*, arXiv:1703.00965
- Blandford, R. D., & Königl, A. 1979, *ApJ*, 232, 34
- Blandford, R. D., & Rees, M. J. 1974, *MNRAS*, 169, 395
- Bloom, J. S., Giannios, D., Metzger, B. D., et al. 2011, *Science*, 333, 203
- Bower, G. C., Metzger, B. D., Cenko, S. B., Silverman, J. M., & Bloom, J. S. 2013, *ApJ*, 763, 84
- Bright, J. S., Fender, R. P., Motta, S. E., et al. 2018, *MNRAS*, 475, 4011
- Brown, G. C., Levan, A. J., Stanway, E. R., et al. 2015, *MNRAS*, 452, 4297
- Brown, J. S., Holoien, T. W.-S., Auchettl, K., et al. 2017, *MNRAS*, 466, 4904
- Burbidge, G. R. 1956, *ApJ*, 124, 416
- Burrows, D. N., Kennea, J. A., Ghisellini, G., et al. 2011, *Nature*, 476, 421
- Cenko, S. B., Krimm, H. A., Horesh, A., et al. 2012, *ApJ*, 753, 77
- Chatterjee, R., Marscher, A. P., Jorstad, S. G., et al. 2011, *ApJ*, 734, 43
- Chevalier, R. A. 1998, *ApJ*, 499, 810
- Coughlin, E. R., & Begelman, M. C. 2014, *ApJ*, 781, 82
- Croston, J. H., Hardcastle, M. J., Harris, D. E., et al. 2005, *ApJ*, 626, 733
- Crumley, P., Ceccobello, C., Connors, R. M. T., & Cavecchi, Y. 2017, *ArXiv e-prints*, arXiv:1703.02842
- Dai, L., McKinney, J. C., & Miller, M. C. 2015, *ApJ*, 812, L39
- Esquej, P., Saxton, R. D., Komossa, S., et al. 2008, *A&A*, 489, 543
- Falcke, H., & Biermann, P. L. 1995, *A&A*, 293, 665
- Falcke, H., K rding, E., & Markoff, S. 2004, *A&A*, 414, 895
- Falcke, H., Malkan, M. A., & Biermann, P. L. 1995, *A&A*, 298, 375
- Falcke, H., Bower, G. C., Lobanov, A. P., et al. 1999, *ApJ*, 514, L17
- French, K. D., Arcavi, I., & Zabludoff, A. 2016, *ApJ*, 818, L21
- Gallo, E., Fender, R. P., & Pooley, G. G. 2003, *MNRAS*, 344, 60
- Gaskell, C. M., & Peterson, B. M. 1987, *ApJS*, 65, 1
- Generozov, A., Mimica, P., Metzger, B. D., et al. 2017, *MNRAS*, 464, 2481
- Gezari, S., Heckman, T., Cenko, S. B., et al. 2009, *ApJ*, 698, 1367
- Giannios, D., & Metzger, B. D. 2011, *MNRAS*, 416, 2102
- Harwood, J. J., Croston, J. H., Intema, H. T., et al. 2016, *MNRAS*, 458, 4443
- Heinz, S., & Sunyaev, R. A. 2003, *MNRAS*, 343, L59
- Herrnstein, J. R., Moran, J. M., Greenhill, L. J., et al. 1997, *ApJ*, 475, L17
- . 2016b, *MNRAS*, 455, 2918
- Irwin, J. A., Henriksen, R. N., Krause, M., et al. 2015, *ApJ*, 809, 172
- Kara, E., Miller, J. M., Reynolds, C., & Dai, L. 2016, *Nature*, 535, 388
- Kataoka, J., & Stawarz, L. 2005, *ApJ*, 622, 797
- Ker, L. M., Best, P. N., Rigby, E. E., R ttgering, H. J. A., & Gendre, M. A. 2012, *MNRAS*, 420, 2644
- Komossa, S. 2002, in *Reviews in Modern Astronomy*, Vol. 15, *Reviews in Modern Astronomy*, ed. R. E. Schielicke, 27
- Krolik, J., Piran, T., Svirski, G., & Cheng, R. M. 2016, *ApJ*, 827, 127
- Levan, A. J., Tanvir, N. R., Cenko, S. B., et al. 2011, *Science*, 333, 199
- Levan, A. J., Tanvir, N. R., Brown, G. C., et al. 2016, *ApJ*, 819, 51
- Lodato, G., King, A. R., & Pringle, J. E. 2009, *MNRAS*, 392, 332
- Lodato, G., & Rossi, E. M. 2011, *MNRAS*, 410, 359
- Markoff, S., Nowak, M. A., & Wilms, J. 2005, *ApJ*, 635, 1203
- Marscher, A. P. 1980, *ApJ*, 235, 386
- Marscher, A. P., & Gear, W. K. 1985, *ApJ*, 298, 114
- Marscher, A. P., Jorstad, S. G., G mez, J.-L., et al. 2002, *Nature*, 417, 625
- Merloni, A., Heinz, S., & di Matteo, T. 2003, *MNRAS*, 345, 1057
- Metzger, B. D., Giannios, D., & Mimica, P. 2012, *MNRAS*, 420, 3528
- Miller, J. M., & G ltekin, K. 2011, *ApJ*, 738, L13
- Miller, J. M., Kaastra, J. S., Miller, M. C., et al. 2015, *Nature*, 526, 542
- Mimica, P., Giannios, D., Metzger, B. D., & Aloy, M. A. 2015, *MNRAS*, 450
- Nakar, E., & Piran, T. 2011, *Nature*, 478, 82
- Pacholczyk, A. G. 1970, *Radio astrophysics. Nonthermal processes in galactic and extragalactic sources* (Freeman and Co., San Francisco)
- Pasham, D. R., Cenko, S. B., Sadowski, A., et al. 2017, *ApJ*, 837, L30
- Pasham, D. R., Cenko, S. B., Levan, A. J., et al. 2015, *ApJ*, 805, 68
- Perlman, E. S., Meyer, E. T., Wang, Q. D., et al. 2017, *ApJ*, 842, 126
- Peterson, B. M., Ferrarese, L., Gilbert, K. M., et al. 2004, *ApJ*, 613, 682
- Phinney, E. S. 1989, in *IAU Symposium*, Vol. 136, *The Center of the Galaxy*, ed. M. Morris, 543
- Piran, T. 2004, *Reviews of Modern Physics*, 76, 1143
- Prieto, J. L., Kr hler, T., Anderson, J. P., et al. 2016, *ApJ*, 830, L32
- Rawlings, S., & Saunders, R. 1991, *Nature*, 349, 138
- Readhead, A. C. S., Cohen, M. H., Pearson, T. J., & Wilkinson, P. N. 1978, *Nature*, 276, 768
- Rees, M. J. 1988, *Nature*, 333, 523
- Remillard, R. A., & McClintock, J. E. 2006, *ARA&A*, 44, 49
- Romero-C nizales, C., Mattila, S., Alberdi, A., et al. 2011, *MNRAS*, 415, 2688
- Romero-C nizales, C., Prieto, J. L., Chen, X., et al. 2016, *ApJ*, 832, L10
- Saxton, R. D., Read, A. M., Komossa, S., et al. 2017, *A&A*, 598, A29
- S dowski, A., Bursa, M., Abramowicz, M., et al. 2011, *A&A*, 532, A41
- S dowski, A., & Narayan, R. 2016, *MNRAS*, 456, 3929
- Shappee, B. J., Prieto, J. L., Grupe, D., et al. 2014, *ApJ*, 788, 48
- Tchekhovskoy, A., Metzger, B. D., Giannios, D., & Kelley, L. Z. 2014, *MNRAS*, 437, 2744
- Tremaine, S., Gebhardt, K., Bender, R., et al. 2002, *ApJ*, 574, 740
- van der Laan, H. 1966, *Nature*, 211, 1131
- van Velzen, S., Falcke, H., & K rding, E. 2015, *MNRAS*, 446, 2985
- van Velzen, S., Frail, D. A., K rding, E., & Falcke, H. 2013, *A&A*, 552, A5
- van Velzen, S., K rding, E., & Falcke, H. 2011, *MNRAS*, 417, L51
- van Velzen, S., Mendez, A. J., Krolik, J. H., & Gorjian, V. 2016a, *ApJ*, 829, 19
- van Velzen, S., Farrar, G. R., Gezari, S., et al. 2011, *ApJ*, 741, 73
- van Velzen, S., Anderson, G. E., Stone, N. C., et al. 2016b, *Science*, 351, 62
- Wevers, T., van Velzen, S., Jonker, P. G., et al. 2017, *MNRAS*, 471, 1694
- White, R. J., & Peterson, B. M. 1994, *PASP*, 106, 879
- Yuan, F., & Cui, W. 2005, *ApJ*, 629, 408
- Zauderer, B. A., Berger, E., Soderberg, A. M., et al. 2011, *Nature*, 476, 425

TABLE A1
 X-RAY FLUX AND COUNT RATES.

ObsID ^a	MJD ^b	X-ray flux ^c	X-ray count rate ^d	Exposure ^e	Pile-up radius ^f	χ^2/dof^g
00033539001	56991.483	1.376±0.136	0.286±0.010	2952	5	1.34/21
00033539002	56993.918	1.809±0.201	0.320±0.011	2812	6	1.11/18
00033539003	56995.312	1.056±0.156	0.260±0.009	2997	7	1.10/10
00033539004	56998.260	1.504±0.118	0.270±0.010	2952	4	0.77/28
00033539005	57001.638	1.725±0.138	0.316±0.010	2892	4	1.43/25
00033539006	57004.128	1.515±0.155	0.278±0.015	1179	7	-/-
00033539007	57007.297	1.881±0.138	0.386±0.011	2944	4	0.76/29
00033539008	57010.836	1.841±0.172	0.406±0.012	3044	6	1.20/21
00033539009	57013.100	1.849±0.135	0.350±0.011	3122	4	1.50/28
00033539010	57016.093	1.837±0.172	0.247±0.009	2829	5	0.89/23
00033539011	57019.577	1.694±0.111	0.373±0.011	3169	3	1.60/28
00033539012	57022.746	1.419±0.128	0.248±0.009	2764	4	0.73/23
00033539014	57029.583	1.567±0.092	0.339±0.009	3773	3	1.38/35
00033539015	57033.145	1.515±0.180	0.387±0.015	1681	5	1.09/14
00033539016	57036.111	1.739±0.139	0.379±0.014	2075	3	1.13/26
00033539017	57039.235	1.440±0.090	0.314±0.011	2797	2	0.77/33
00033539018	57042.297	1.369±0.106	0.328±0.013	1943	2	1.61/29
00033539019	57045.625	1.358±0.101	0.306±0.011	2325	2	1.09/28
00033539020	57048.822	1.263±0.180	0.310±0.011	2489	7	1.32/11
00033539021	57051.535	1.173±0.185	0.267±0.011	2342	7	1.78/11
00033539022	57054.140	1.124±0.128	0.268±0.010	2909	5	1.07/16
00033539023	57057.561	1.154±0.138	0.307±0.010	2909	6	0.43/14
00033539024	57060.166	0.968±0.146	0.261±0.010	2565	7	1.46/10
00033539025	57065.850	0.924±0.143	0.206±0.011	1831	5	0.55/9
00033539026	57068.771	0.780±0.121	0.209±0.011	1581	7	-/-
00033539027	57071.738	0.999±0.140	0.267±0.010	2482	6	0.98/11
00033539028	57074.911	0.885±0.126	0.220±0.009	2847	6	0.39/10
00033539029	57077.634	0.994±0.136	0.127±0.007	2470	5	1.08/12
00033539030	57081.190	0.948±0.138	0.219±0.009	3012	6	0.88/10
00033539032	57086.918	0.958±0.161	0.238±0.010	2215	6	1.73/9
00033539033	57089.382	1.244±0.135	0.216±0.009	2857	5	0.70/18
00033539034	57099.388	1.379±0.192	0.290±0.014	1471	6	-/-
00033539035	57102.656	1.004±0.122	0.211±0.010	2118	4	0.97/14
00033539036	57105.308	0.548±0.092	0.115±0.012	759	4	-/-
00033539037	57108.768	0.918±0.151	0.223±0.010	2223	7	-/-
00033539038	57111.934	0.926±0.141	0.225±0.010	2442	6	0.85/10
00033539039	57114.090	1.000±0.166	0.243±0.012	1591	7	-/-
00033539040	57117.683	0.721±0.127	0.221±0.010	2258	7	-/-
00033539041	57120.318	0.701±0.115	0.215±0.010	2035	5	0.52/8
00033539042	57123.540	0.652±0.120	0.174±0.009	2225	5	-/-
00033539043	57126.244	0.682±0.116	0.182±0.009	2397	5	0.70/7
00033539045	57129.401	0.799±0.084	0.196±0.011	1768	0	0.58/18
00033539046	57132.561	0.578±0.075	0.143±0.008	2213	2	0.89/13
00033539047	57136.561	0.585±0.077	0.162±0.011	1443	0	1.10/12
00033539048	57139.348	0.837±0.100	0.153±0.008	2223	2	0.83/13
00033539049	57147.598	0.712±0.082	0.142±0.008	2317	2	1.29/15
00033539050	57150.257	0.817±0.066	0.183±0.008	2642	0	0.79/26
00033539051	57153.487	0.741±0.068	0.177±0.008	2490	1	1.01/22
00033539052	57156.349	0.666±0.080	0.159±0.010	1656	4	-/-
00033539053	57173.107	0.656±0.068	0.156±0.009	1945	0	0.67/18
00033539054	57176.134	0.630±0.070	0.177±0.010	1845	0	1.18/15
00033539055	57179.029	0.498±0.080	0.140±0.014	691	2	-/-
00033539056	57182.466	0.630±0.090	0.136±0.011	1134	0	0.63/10
00033539057	57186.056	0.539±0.068	0.115±0.008	1666	0	1.29/13
00033539059	57191.846	0.602±0.065	0.133±0.008	2160	0	0.60/18
00033539060	57195.196	0.592±0.070	0.121±0.007	2298	2	1.07/15
00033539061	57200.383	0.532±0.082	0.132±0.010	1301	1	0.96/9
00033539062	57203.808	0.424±0.055	0.134±0.009	1836	0	0.55/11
00033539063	57226.618	0.387±0.054	0.120±0.008	2008	0	0.74/11
00033539064	57230.374	0.423±0.075	0.132±0.012	954	0	-/-
00033539065	57236.471	0.404±0.059	0.124±0.007	2352	2	0.43/9
00033539067	57242.121	0.452±0.053	0.106±0.007	2427	0	1.08/14
00033539068	57246.908	0.342±0.047	0.075±0.006	2382	0	0.54/11
00033539069	57340.746	0.397±0.051	0.063±0.004	3251	0	0.66/12
00033539070	57351.806	0.247±0.054	0.050±0.005	2155	0	-/-
00033539071	57354.699	0.227±0.039	0.046±0.004	2472	0	1.43/8
00033539072	57357.365	0.322±0.048	0.066±0.005	2442	0	0.41/8
00033539073	57360.259	0.362±0.055	0.090±0.007	1973	0	0.61/9
00033539074	57363.952	0.366±0.048	0.096±0.006	2470	0	0.41/10
00033539075	57366.941	0.393±0.054	0.073±0.005	2492	0	1.37/11
00033539076	57369.828	0.370±0.064	0.069±0.005	2457	2	-/-
00033539077	57372.213	0.331±0.060	0.062±0.006	1898	0	-/-
00033539078	57375.538	0.285±0.059	0.061±0.006	1838	2	-/-
00033539079	57378.412	0.358±0.059	0.077±0.006	1933	0	1.06/8

TABLE A1 — *Continued*

ObsID ^a	MJD ^b	X-ray flux ^c	X-ray count rate ^d	Exposure ^e	Pile-up radius ^f	χ^2/dof ^g
00033539080	57383.201	0.133±0.042	0.029±0.007	531	0	-/-
00033539082	57411.445	0.281±0.056	0.071±0.006	1766	2	-/-
00033539084	57417.731	0.277±0.044	0.070±0.006	2125	0	0.94/8
00033539085	57423.003	0.321±0.072	0.081±0.011	684	0	-/-
00033539086	57426.465	0.157±0.048	0.040±0.010	419	0	-/-
00033539087	57427.720	0.279±0.055	0.070±0.006	1988	0	-/-
00033539088	57429.666	0.104±0.030	0.026±0.006	731	0	-/-
00033539089	57432.788	0.194±0.040	0.049±0.005	1806	2	-/-
00033539090	57435.706	0.199±0.041	0.050±0.005	1953	2	-/-
00033539091	57519.777	0.182±0.038	0.046±0.005	2120	0	-/-
00033539092	57522.502	0.139±0.029	0.035±0.004	2342	0	-/-
00033539093	57526.691	0.142±0.030	0.036±0.004	2075	0	-/-
00033539094	57542.648	0.128±0.029	0.032±0.004	1733	2	-/-
00033539095	57545.454	0.127±0.040	0.032±0.008	474	0	-/-
00033539096	57546.365	0.147±0.033	0.037±0.005	1441	2	-/-
00033539097	57550.094	0.160±0.034	0.041±0.005	1818	2	-/-
00033539098	57554.342	0.097±0.022	0.025±0.004	1998	2	-/-
00033539099	57718.004	0.086±0.019	0.022±0.003	2410	0	-/-
00033539100	57819.598	0.050±0.020	0.013±0.005	606	0	-/-
00033539101	57820.399	0.055±0.014	0.014±0.003	1910	0	-/-
00033539102	57821.936	0.096±0.023	0.024±0.004	1688	0	-/-
00033539103	57826.844	0.029±0.010	0.007±0.002	1873	1	-/-
00033539104	57828.563	0.071±0.021	0.018±0.004	1029	0	-/-
00033539105	57833.492	0.089±0.025	0.022±0.005	954	0	-/-

NOTE. — ^a*Swift*-assigned observation IDs. ^bModified Julian Date. ^cThe X-ray fluxes were estimated from 0.3–1.0 keV bandpass and are in the units of 10^{-11} erg s⁻¹ cm⁻². The uncertainties indicate both the lower and the upper 1σ confidence levels. ^dPSF-corrected X-ray count rates were also estimated from 0.3–1.0 keV bandpass and are in the units of counts per second. ^eExposure time in seconds. ^fInner exclusion radius in units of XRT pixels (1 pixel \approx 2.36") to mitigate photon pileup. This inner exclusion radius was determined by manually fitting the PSF in each exposure following the methodology outlined in the *Swift*/XRT user guide (see sec. 2.2). ^gThe reduced χ^2 along with the dof are indicated in the last column. For exposures marked by -/-, because the pile-up corrected counts were less than 100, the flux was estimated by scaling by the count rate of the nearest observation with spectral flux estimate (see sec. 2.2).